Performance Evaluation for Ground-Based Integrity Monitor Network

Yu-Fang Lai, Juan Blanch, Todd Walter
Stanford University

BIOGRAPHY

Yu-Fang Lai is a Ph.D. candidate at Stanford GPS Lab. He received Bachelor's degree in Aero/Astro from National Cheng-Kung University in 2020, and Master's degree in Aero/Astro from Stanford in 2022.
Juan Blanch is a senior research engineer at Stanford University. He is a graduate of Ecole Polytechnique in France, he holds an M.S. degree in electrical engineering and a Ph.D. degree in aeronautics and astronautics from Stanford University.
Todd Walter is a Professor at Stanford University and the faculty of Stanford GPS Lab. He received his B.S. degree in physics from Rensselaer Polytechnic Institute and his Ph.D. degree in 1993 from Stanford University.

ABSTRACT

In this paper, we address the issue of evaluating the performance of integrity monitors without pseudorange data. Specifically, we simulate the evolution of geometry with almanac data. It allows us to rapidly evaluate the error bounds of arbitrary numbers and locations of receiver networks. The error bounds of the PPP users are computed by solving steady-state Algebraic Riccati Equation of the Kalman filter. We also derived the information form of the satellite error at steady-state for the integrity monitor. Since the priors of the simulation is identical to the fault-tolerant filter with real data, the error bounds from the simulation produce the lower bound performance of the networks. In real data there are events such as cycle slips that would temporarily disrupt the estimations, which would degrade the performance. We compare the error bounds between the simulation and real data from a network of 56 reference stations to confirm the lower bound property of the simulated result. This work supports selecting and placing reference stations when designing monitor networks.

I. INTRODUCTION

Precise Point Positioning (PPP) is a positioning technique that can achieve decimeter level of positioning accuracy for kinematic users of Global Navigation Satellite System (GNSS), and centimeter level for static users, with only the code and carrier phase pseudorange measurements. The extremely accurate positioning results rely on the sophisticated modeling of the pseudorange errors (Zumberge et al., 1997), and the use of precise corrections such as precise satellite clock bias and precise ephemeris. The modeling of the pseudorange errors include but are not limited to: atmospheric effects, antenna phase biases, antenna phase variations, differential code bias, solid earth tides, gravitational deformation and etc. In addition to error modeling, PPP also considers temporal correlations and the prior of the models when estimating the user position. The typical approach of realizing PPP standard utilizes Extended-Kalman Filter (EKF) (Welch et al., 1995) to estimate the user position and the associated pseudorange errors. In addition to the error modelings, which can be accomplished independently in a standalone GNSS receiver, the precise corrections the PPP users apply are entirely reliant on the service providers. Without the precise satellite clock and precise ephemeris, the accuracy of the positioning result degrades to 1-3 m if using the navigation message broadcast in the GNSS signals. The integrity and the accuracy of PPP users therefore completely rely on the precise correction information the PPP service providers broadcast.

In the previous works Lai et al. (2024, 2025a,b), we demonstrated that the integrity of the PPP users can be protected from arbitrary type of satellite clock and ephemeris faults, while maintaining decimeter level of positioning accuracy using a ground-based integrity monitor. The integrity monitor estimates the User Range Errors (URE) induced from any type of satellite clock and ephemeris fault/anomaly and is causal in time. Since the users of PPP and the monitor observe the same satellite faults, the users can apply the UREs from the integrity monitor as additional corrections to the measurement models to compensate for the effect of satellite faults on user range measurements and therefore protect the integrity of the positioning result. The integrity monitor allows the service provider of PPP to claim integrity on the correction information they provide to the users. In Lai et al. (2025b), 56 GNSS receivers from International GNSS Service (IGS) are selected to the monitor network. It was shown that the network of 56 receivers is capable of monitoring the entire GPS constellation without interruption, and the users can achieve down to $\sim$1 m horizontal and $\sim$2 m vertical protection level at JPLM station in Los Angeles. All of which are demonstrated using real GNSS measurements provided from the IGS.

In this paper, we define and evaluate the performance of the entire integrity monitor network. Since the goal of the integrity

monitor is to provide integrity for the PPP users, the protection level of the users indicates how well the integrity monitor can provide integrity to the corresponding users while maintaining their accuracy. As a result, we use protection level at the potential user locations on Earth to quantify the performance of a ground-based network. Specifically, the protection levels are computed from the steady-state Kalman filter with integrity information from the integrity network that is under evaluation. The steady-state Kalman filter removes the temporal relations of the measurements, which allows users at difference locations to concentrate on the geometric relations between the satellites.

In addition to the evaluation of protection level at steady-state at potential user locations, a simulation system of integrity monitor based on the almanac data is also proposed. The almanac can achieve an accuracy of 1$\sim$2 km in terms of the orbital trajectory of the satellites. The orbital errors are too large for the state estimation of UREs, but are sufficient for the uncertainty estimate of the integrity network, for which all we need for the computation of protection level. We derived an approximation of the uncertainty of the satellite clock and ephemeris errors in the form of steady-state information filter with only the almanac data. Combined with the steady-state protection level from the users, it allows a full evaluation of the performance of an integrity monitor without the need of real GNSS data. The performance of a integrity network evaluated from the full simulation serves as a lower bound for the actual performance of the network. The results of the full simulation and real data are compared to understanding the gap between the lower bound and the GNSS data from real network.

This paper is structured as follows: Sec.II formulates measurement models of the IMS and PPP users and introduces the integrity information used by the users. Sec.III explains the use of steady-state Kalman and Information filter and derives derive the steady-state approximation of the covariance of the satellite errors that can greatly reduce the computation. Sec.IV introduces the dataset used in this paper. Sec.V shows the global steady-state VPL from actual receiver network, simulated data with almanac, and the baseline percentage of the actual and simulated VPL. Finally, Sec.VI concludes the paper.

II. BACKGROUND

1. Measurement Models of PPP Users

$$\rho_{\text{IF},r}^{(k)} = \| \overrightarrow{x}_{sat}^{(k)} - \overrightarrow{x}_{pos,r} \| + \left(b_r - b_{sat}^{(k)} \right) + m_r^{(k)} \nabla \hat{T}_r + R_{\rho,r}^{(k)} + \epsilon_r^{(k)} \tag{1}$$

$$\phi_{\text{IF},r}^{(k)} = \| \overrightarrow{x}_{sat}^{(k)} - \overrightarrow{x}_{pos,r} \| + \left(b_r - b_{sat}^{(k)} \right) + m_r^{(k)} \nabla \hat{T}_r + A^{(k)} + R_{\phi,r}^{(k)} + \epsilon_r^{(k)} \tag{2}$$

Eq.1 and Eq.2 are the dual-frequency ionospheric free combination of code-phase and carrier-phase pseudorange models from the k^{th} satellite at r^{th} receiver in Earth-Center Earth-Fixed (ECEF) coordinate, respectively. $\overrightarrow{x}_s^{(k)} \in \mathbb{R}^{3\times 1}$ is the ephemeris, $\overrightarrow{x}_{pos,r}$ is the position of the receiver, b_r is the receiver clock bias, $b_{sat}^{(k)}$ is the satellite clock bias, $m_r^{(k)}$ is the mapping function for the tropospheric delay and $\nabla \hat{T}_r$ is the wet delay error. $R_\rho^{(k)}$ and $R_\phi^{(k)}$ consist of all the modeled effects for code and carrier phase respectively, including satellite antenna phase center offset, satellite/receiver antenna phase variation, relativistic effects, solid earth tide modeling, ocean loading, modeled tropospheric delay, Sagnac Effect, group delay variation for code phase measurements and phase wind up for carrier phase measurements. Finally, $\epsilon_r^{(k)}$ is all the un-modeled effects to the measurement models and is assumed to be normally distributed. Eq.1 and Eq.2 are the measurement models used PPP users adopt in this paper.

Therefore, we can define the state vector of a single GNSS receiver as:

$$\overrightarrow{x_r} = \begin{bmatrix} x_r \\ y_r \\ z_r \\ v_{x,r} \\ v_{y,r} \\ v_{z,r} \\ b_r \\ \nabla b_r \\ \nabla \hat{T}_r \\ A_r^{(1)} \\ \vdots \\ A_r^{(k)} \end{bmatrix} \tag{3}$$

2. Measurement Models of Fault-Tolerant Filter

$$\rho_{\text{IF},r}^{(k)} = \| \overrightarrow{x}_{sat}^{(k)} - \overrightarrow{x}_{pos,r} + \Delta\overrightarrow{\gamma}^{(k)} \| + \left(b_r - b_{sat}^{(k)} \right) + m_r^{(k)} \nabla \hat{T}_r + R_{\rho,r}^{(k)} + \zeta^{(k)} + \epsilon_r^{(k)} \tag{4}$$

$$\phi_{\text{IF},r}^{(k)} = \| \overrightarrow{x}_{sat}^{(k)} - \overrightarrow{x}_{pos,r} + \Delta\overrightarrow{\gamma}^{(k)} \| + \left(b_r - b_{sat}^{(k)} \right) + m_r^{(k)} \nabla \hat{T}_r + A^{(k)} + R_{\phi,r}^{(k)} + \zeta^{(k)} + \epsilon_r^{(k)} \tag{5}$$

Eq.4 and Eq.5 are the measurement models of the fault-tolerant filter operated in the IMS. They are similar to Eq.1 and Eq.2 except the additional error states, $\zeta^{(k)}$ and $\Delta\overrightarrow{\gamma}^{(k)}$, that account for the satellite clock errors and ephemeris errors, respectively. These two states are assumed without any prior and reset to zero at each time-update with their process noise as large as the receiver clock bias states. This is reflecting the fact that we have no prior knowledge about when and what type of satellite clock and ephemeris faults can occur. It is shown in Lai et al. (2024) that this formulation can accurately capture the satellite faults in the range domain at the potential user locations.

The state vector of the fault-tolerant filter is then:

$$\overrightarrow{x} = \begin{bmatrix} \overrightarrow{x_1} \\ \overrightarrow{x_2} \\ \vdots \\ \overrightarrow{x_r} \\ \vdots \\ \overrightarrow{x_n} \\ \overrightarrow{D_1} \\ \overrightarrow{D_2} \\ \vdots \\ \overrightarrow{D_j} \\ \vdots \\ \overrightarrow{D_m} \end{bmatrix} \tag{6}$$

where there are n receivers and m satellites within the integrity monitor, and $\overrightarrow{D_j}$ is defined as the satellite clock and ephemeris errors:

$$\overrightarrow{D_j} = \begin{bmatrix} \zeta_j \\ \Delta\overrightarrow{\gamma}_j \end{bmatrix} \tag{7}$$

3. Integrity Information

The UREs and its' Error Bounds (standard deviations) can be obtained through the process of projecting the estimates of $\zeta^{(k)}$ and $\Delta\overrightarrow{\gamma}^{(k)}$ onto the Line-Of-Sight (LOS) of the potential user location.

The LOS vector from the position of the k^{th} satellite, $\overrightarrow{x}_{sat}^{(k)}$, to a potential user location, $\overrightarrow{x}_{pos,u}$, is a unit vector:

$$\overrightarrow{l}_{k,u} = \frac{\left(\overrightarrow{x}_{sat}^{(k)} - \overrightarrow{x}_{pos,u} \right)}{| \overrightarrow{x}_{sat}^{(k)} - \overrightarrow{x}_{pos,u} |}$$

The UREs, $\beta_u^{(k)}$, at the position of u is therefore:

$$\beta_u^{(k)} = \begin{bmatrix} 1 \\ \overrightarrow{l}_{k,u} \end{bmatrix}^T \cdot \begin{bmatrix} \zeta^{(k)} \\ \Delta\overrightarrow{\gamma}^{(k)} \end{bmatrix} \tag{8}$$

Similarly, the standard deviation of $\beta_u^{(k)}$, $\sigma_u^{(k)}$, is obtained through the linear transformation of the projection:

$$\sigma_u^{(k)^2} = \begin{bmatrix} 1 \\ \overrightarrow{l} \end{bmatrix}_{k,u}^T \cdot COV\left(\begin{bmatrix} \zeta^{(k)} \\ \Delta\overrightarrow{\gamma}^{(k)} \end{bmatrix} \right) \cdot \begin{bmatrix} 1 \\ \overrightarrow{l} \end{bmatrix}_{k,u} \tag{9}$$

Here, we define the pair of $\beta_u^{(k)}$ and $\sigma_u^{(k)}$ as integrity information that the IMS is providing to the users. The PPP users receive the UREs and their Error Bounds of the GPS constellation as extra corrections in their pseudorange model.

Users can simply apply the corrections to the measurement models:

$$\tilde{\rho}_{\text{IF},r}^{(k)} = \| \overrightarrow{x}_{sat}^{(k)} - \overrightarrow{x}_{pos,r} \| + \left(b_r - b_{sat}^{(k)} \right) + m_r^{(k)} \nabla \hat{T}_r + R_{\rho,r}^{(k)} + \beta_u^{(k)} + \epsilon_r^{(k)} \tag{10}$$

$$\tilde{\phi}_{\text{IF},r}^{(k)} = \| \overrightarrow{x}_{sat}^{(k)} - \overrightarrow{x}_{pos,r} \| + \left(b_r - b_{sat}^{(k)} \right) + m_r^{(k)} \nabla \hat{T}_r + A^{(k)} + R_{\phi,r}^{(k)} + \beta_u^{(k)} + \epsilon_r^{(k)} \tag{11}$$

The associated measurement noise is also inflated with the uncertainty of the UREs:

$$R_{\tilde{\rho}_{\text{IF},r}^{(k)}} = R_{\rho_{\text{IF},r}^{(k)}} + \sigma_u^{(k)^2} \tag{12}$$

$$R_{\tilde{\phi}_{\text{IF},r}^{(k)}} = R_{\phi_{\text{IF},r}^{(k)}} + \sigma_u^{(k)^2} \tag{13}$$

4. Protection Level

Given that any potential satellite clock or ephemeris faults are protected by the integrity information, the protection level is simply the constant multiple of user position sigma.

$$PL_e = K \cdot \sigma_e \tag{14}$$

$$K = Q^{-1}\left(1 - \frac{PHMI}{2}\right) \tag{15}$$

where PL_e is the protection level in e direction (i.e. vertical or horizontal), σ_e is the 1-sigma uncertainty of position estimates from the user filter, Q is CDF of normal distribution and PHMI is Probability of Hazardously Misleading Information. PHMI is assumed to be 10^{-7} in this paper.

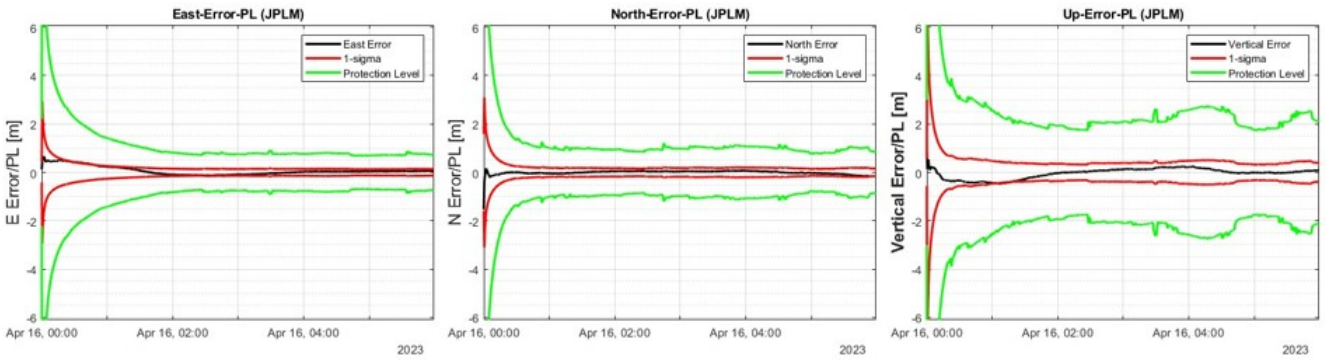

Figure 1: Performance of JPLM user.

Fig.1 is the performance of a PPP user at JPLM station with integrity information provided by the 56-station network introduced in Fig.3. It includes the position errors in East-North-Up directions, 1-sigma position uncertainties and the associated protection levels. The protection levels are simply the constant multiples of the user's 1-sigma uncertainties.

5. Covariance update of Kalman Filter

Standard Extended Kalman-Filter consists of two steps of updates: Time-Update and Measurement-Update, which are the estimation based on the dynamic and measurement models respectively.

Time-Update:

$$\overrightarrow{\mu}_{t|t-1} = A_{t-1}\overrightarrow{\mu}_{t-1|t-1} + B_{t-1}\overrightarrow{u}_{t-1} \tag{16}$$

$$\Sigma_{t|t-1} = A_{t-1}\Sigma_{t-1|t-1}A_{t-1}^T + Q_{t-1} \tag{17}$$

Measurement-Update:

$$\overrightarrow{\mu}_{t|t} = \overrightarrow{\mu}_{t|t-1} + K_t\left(\overrightarrow{y}_t - C_t\overrightarrow{\mu}_{t|t-1}\right) \tag{18}$$

$$\Sigma_{t|t} = \Sigma_{t|t-1} - K_tC_t\Sigma_{t|t-1} \tag{19}$$

$$K_t = \Sigma_{t|t-1}C_t^T\left(C_t\Sigma_{t|t-1}C_t^T + R_t\right)^{-1} \tag{20}$$

where $\overrightarrow{\mu}$ is the mean of the Gaussian estimate of the system state, and Σ is the covariance of the estimate. K_t is the Kalman Gain, which represents the mapping of the measuring and modeling of the system.

III. STEADY-STATE KALMAN AND INFORMATION FILTER

In standard Kalman-Filter, the computation of the protection level for the PPP users is both spatially and temporally correlated. The spatial correlation emerges from the LOS geometry between the users and the satellites, and the temporal correlation is from the converging process of the sequential update from Kalman filter. In general, the performance of a PPP user is considered useful only after convergence. That is, the performance of an integrity monitor when evaluating at the users can only be comparable if the temporal effects are removed. As a result, in this paper we focus on the spatial correlations from the integrity monitor to the user by computing the users' protection level at steady-state.

1. Steady-State Covariance from DARE:

The equation of steady-state covariance is derived by substituting Eq.17 and 20 into Eq.19:

$$\Sigma = A\Sigma A^T + Q - \left(A\Sigma A^TC^T + QC^T\right)\left(CA\Sigma A^TC^T + CQC^T + R\right)^{-1}\left(CA\Sigma A^T + CQ\right) \tag{21}$$

where Σ is the stead-state covariance, and the subscript t is abbreviated for simplicity. Equation is also known as a form of Discrete-Time Algebraic Riccati Equation (DARE) that can be solved efficiently in Matlab with its numerical solver, $idare$. Σ in Eq.21 represents the uncertainty of the defined state given the dynamic model (A), process noise (Q), measurement model (C) and measurement noise (R) at steady-state without the influence of the temporal correlation from the converging process.

The computation of the vertical protection level for any potential user is straightforward. Given the priors of the user filter and the associated integrity information, one can solve Eq.21 for the position covariance Σ_{xyz}, and thereafter the protection level at steady-state from Eq.14 at steady-state.

Due to the fact that the process noise of ambiguity states is zero, meaning they will converge to zero at steady-state:

$$\Sigma = \begin{bmatrix} \sigma_x^2 & \cdots & \sigma_{x,\nabla\hat{T}_r} & \sigma_{x,A_r^{(1)}} & \cdots & \sigma_{x,A_r^{(k)}} \\ \vdots & \ddots & \vdots & \vdots & \ddots & \vdots \\ \sigma_{\nabla\hat{T}_r,x} & \cdots & \sigma^2_{\nabla\hat{T}_r} & \sigma_{\nabla\hat{T}_r,A_r^{(1)}} & \cdots & \sigma_{\nabla\hat{T}_r,,A_r^{(k)}} \\ \sigma_{A_r^{(1)},x} & \cdots & \sigma_{A_r^{(1)},\nabla\hat{T}_r} & \sigma^2_{A_r^{(1)}} & \cdots & \sigma_{A_r^{(1)},A_r^{(k)}} \\ \vdots & \ddots & \vdots & \vdots & \ddots & \vdots \\ \sigma_{A_r^{(k)},x} & \cdots & \sigma_{A_r^{(k)},\nabla\hat{T}_r} & \cdots & \cdots & \sigma^2_{A_r^{(k)}} \end{bmatrix} \rightarrow \begin{bmatrix} \sigma_x^2 & \cdots & \sigma_{x,\nabla\hat{T}_r} & 0 & \cdots & 0 \\ \vdots & \ddots & \vdots & \vdots & \ddots & \vdots \\ \sigma_{\nabla\hat{T}_r,x} & \cdots & \sigma^2_{\nabla\hat{T}_r} & 0 & \cdots & 0 \\ 0 & \cdots & 0 & 0 & \cdots & 0 \\ \vdots & \ddots & \vdots & \vdots & \ddots & \vdots \\ 0 & \cdots & 0 & \cdots & \cdots & 0 \end{bmatrix} \tag{22}$$

It is reasonable and numerically beneficial to ignore the ambiguity states for the steady-state covariance computation. The dimension of a PPP user is then reduced to 9 and is consistent regardless of the satellites LOS.

2. Steady-State Information Approximation of Satellite Errors:

Both PPP user and fault-tolerant filters can solve for steady-state covariance using Eq.21. The user can easily compute the steady-state covariance with the simplification of zero ambiguity states, where the dimensionality is limited to 9 for each user. However, even after ignoring ambiguities at steady-state, the dimensionality of the fault-tolerant filter can still be hundreds or thousands depending on the total number of receivers within the network. To reduce the computation of the covariance of the satellite clock and ephemeris errors, we can transform Eq.21 into information form and utilize the fact that no dynamic model for the satellite errors.

We can separate the states correspond to the receiver and satellite error:

$$\Sigma = \begin{bmatrix} \Sigma_{rcv} & \Sigma_{1,2} \\ \Sigma_{2,1} & \Sigma_{sat} \end{bmatrix} \tag{23}$$

$$A = \begin{bmatrix} A_{rcv} & 0 \\ 0 & A_{sat} = 0 \end{bmatrix} \tag{24}$$

$$C = \begin{bmatrix} C_{rcv} & C_{sat} \end{bmatrix} \tag{25}$$

$$Q = \begin{bmatrix} Q_{rcv} & 0 \\ 0 & Q_{sat} \end{bmatrix} \tag{26}$$

where the subscript rcv correspond to the receiver states, sat correspond to the satellite clock and ephemeris errors, $\Sigma_{1,2}$ is the cross-covariance between the receiver and satellite error states, and A_{sat}, is zero since satellite error states have no dynamic model.

Substitute the above expressions into Eq.21, the covariance of the satellite errors, Σ_{sat}, becomes:

$$\Sigma_{sat} = Q_{sat} - Q_{sat}C_{sat}^T \left(C_{rcv}A_{rcv}\Sigma_{rcv}A_{rcv}^T C_{rcv}^T + C_{rcv}Q_{rcv}C_{rcv}^T + C_{sat}Q_{sat}C_{sat}^T + R\right)^{-1} C_{sat}Q_{sat} \tag{27}$$

Approximate the satellite error covariance by simplifying the effect of receiver covariance at steady-state:

$$\Sigma_{sat} \approx Q_{sat} - Q_{sat}C_{sat}^T \left(C_{rcv}Q_{rcv}C_{rcv}^T + C_{sat}Q_{sat}C_{sat}^T + R\right)^{-1} C_{sat}Q_{sat} \tag{28}$$

The reason that we can simplify the receiver covariance is that without the ambiguity state, the uncertainty of the receiver states is dominant by the receiver clock bias, that theoretically has infinite process noise. However, the effect of receiver clock bias is identical to all the satellites across the receivers. Therefore, this simplification is equivalent to assuming all the satellites are equally affected by each of the receiver. In practice, this simplification makes less than 1 millimeter of difference on the sigma of UREs.

Eq. 28 expresses Σ_{sat} entirely with the measurement models for each of the receivers and decouple the correlations between the receiver states that allows fast computation in information form.

Given the gaussian assumption of Kalman Filter, the information matrix is the inverse of the covariance.

$$Y_{sat} = \Sigma_{sat}^{-1} \tag{29}$$

where Y_{sat} is the information matrix of the satellite error.

Invoking **Woodbury Matrix Identity**, Y_{sat} becomes:

$$Y_{sat} = \Sigma_{sat}^{-1} = \left[Q_{sat} - Q_{sat}C_{sat}^T \left(C_{rcv}Q_{rcv}C_{rcv}^T + C_{sat}Q_{sat}C_{sat}^T + R\right)^{-1} C_{sat}Q_{sat}\right]^{-1} \tag{30}$$

$$= Q_{sat}^{-1} + C_{sat}^T \left(C_{rcv}Q_{rcv}C_{rcv}^T + R\right)^{-1} C_{sat} \tag{31}$$

Since each receiver will only affect the LOS satellites, the matrix inversion is equivalent to the sum of each receiver to its LOS satellite errors.

$$Y_{sat} = Q_{sat}^{-1} + \sum_{r=1}^{n} C_{sat,r}^T \left(C_{rcv,r}Q_{rcv,r}C_{rcv,r}^T + R_r\right)^{-1} C_{sat,r} + C_{sat,const}^T R_{const}^{-1} C_{sat,const} \tag{32}$$

where $C_{sat,r}$, $C_{rcv,r}$, R_r correspond to the measurement models and noise of each receiver respectively and independently. $C_{sat,const}$ and R_{const}^{-1} are the zero-mean constraint described in Lai et al. (2024).

Eq.32 computes the information matrix of the satellite error by summing over the contributions of each receiver with their LOS satellites, and finally a matrix inversion to convert the information matrix into covariance that enables the projection to URE. Each receiver would be LOS to $\sim$10s satellites at a time, meaning its relatively lightweight in terms of matrix computation, and the final matrix inversion will have a fix dimensionality of $m \cdot 4$ that only requires to be computed 1 time. This allows extremely efficient evaluation of the steady-state satellite error covariance regardless of the number of total receivers within the network.

IV. DATASET AND ALMANAC

The International GNSS Service, IGS (2026), has 534 GNSS receiver stations world-wide as of January 30th, 2026 and it provides free access to various GNSS products. The number of stations available may vary from day to day due to new stations being introduced, old stations retired, maintenance or events such as power outage.

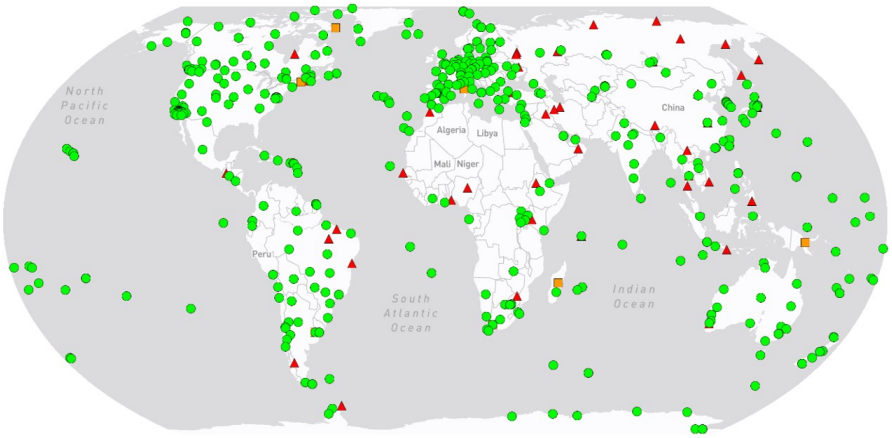

Figure 2: IGS Map and stations. IGS (2026)

In this paper, we used 30(s) interval GNSS measurements from IGS receivers and precise GNSS products, including precise ephemeris (.SP3 file), precise satellite clock bias (.CLK file), Antenna Phase Center Offset (.ATX file) and the estimated receiver position as prior obtained from precise solution (.SNX file).

56 IGS stations are selected to form a ground-based receiver network for the IMS. The station codes are: AC23, ADIS, AGGO, AREG, AREQ, BRMG, CCJ2, CHTI, CRO1, CZTG, DGAR, DRAO, DUND, FAA1, FALK, FLIN, FRDN, HAL1, HARB, HKWS, HOLP, IISC, IQAL, JOG2, KMNM, KRGG, LAMA, LMMF, MAL2, MANA, MCIL, MIKL, MIZU, MKEA, MQZG, NAUS, P051, PIMO, POL2, POVE, RESO, REYK, RIO2, SCTB, SFDM, STHL, SUTH, TASH, TRO1, TSK2, UNBD, VILL, WARK, WSRT, YELL, ZAMB, respectively.

The location of the 56 IGS stations are shown in Fig.3.

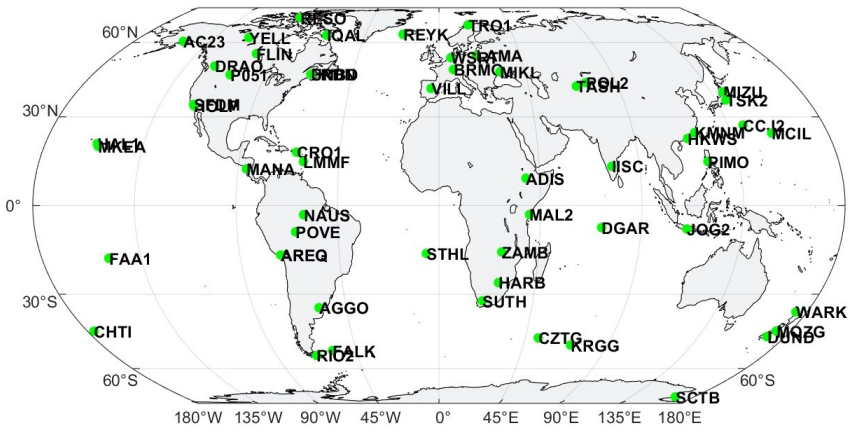

Figure 3: 56 selected IGS stations.

In this experiment, we use GPS L1 and L2, code and carrier phase peudorange measurements collected on April 15$^{\text{th}}$ and 16$^{\text{th}}$, 2023, from the 56 stations to form an Integrity Monitor that monitors the satellite clock and ephemeris errors in the range domain. Observation data on April 15$^{\text{th}}$ is used to converge the fault-tolerant filter of IMS, and the experiments are conducted on April 16$^{\text{th}}$ data. JPLM station, located at $(\text{latitude}, \text{longitude}) = (34.205°, -118.173°)$, at Jet Propulsion Laboratory, is selected to be the actual user in the experiment.

In addition to the precise ephemeris product from the IGS, we also use the GPS almanac to generate the ephemeris for the purpose of simulation. In particular, the ephemeris from the almanac data allows quick evaluation of the receiver to satellite geometry and the covariance computation when combine with Eq.21. This is inspired by Jan et al. (2009).

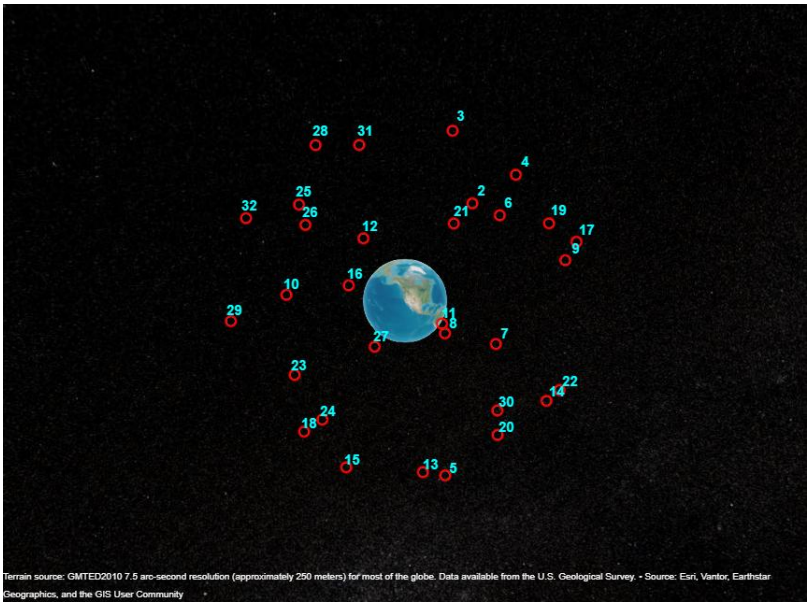

Figure 4: Ephemeris simulation from almanac.

where Fig.4 shows a snapshot of the ephemeris simulation of GPS constellation from the almanac. The red circles are the satellites with the numbers representing the corresponding PRN. The almanac provides the ephemeris in ECEF coordinate using coarse Keplerian orbit model. The accuracy of such orbits is at the scale of $\sim$1 km compare with the precise product. It is not accurate enough for state estimation given the kilometer level of pseudorange errors, but good enough for the approximations of LOS vector and elevation angle, for which the modeling error of $\sim$1 km is normalized by the GPS orbital altitude of $\sim$20200 km. As a result, the almanac itself is suitable for the simulation of the covariance estimates as well as the computation of the

protection levels.

Given the location of the receivers from the integrity monitor, we can then simulate the LOS vectors from the almanac with the elevation angles as the cut-off criteria. To some degree, the protection levels computed from such simulation represent the lower bound of the protection levels that the geometry of the integrity monitor can achieve. In terms of the LOS vectors, the almanac will always be more stable than the actual receivers, which might have events such as cycle slips, loss of track, or multi-path etc. that would degrade the available satellites for the receiver. Even though the LOS vectors from the precise product and almanac are almost identical, the covariance computed from the actual receivers will be greater than or at least equal to the one computed from the almanac given that the only cut-off criteria for the almanac are elevation angle.

V. SIMULATION RESULT

1. Partial Simulation

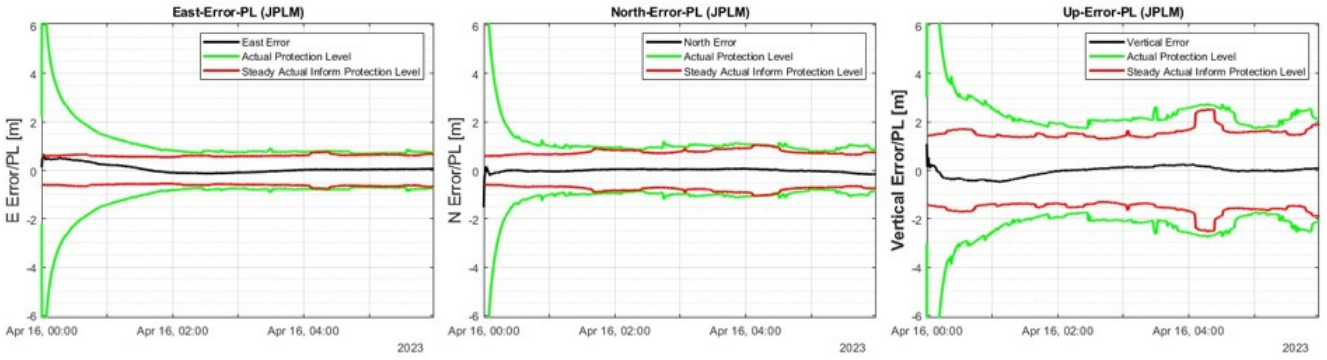

Figure 5: Partial simulation of JPLM user.

Fig.5 is the partial simulation of the JPLM user with the 56-station network. The red lines are the protection levels computed from the simulated PPP user with steady-state Kalman-Filter, i.e. Eq.21. The simulated user still applies actual integrity information from the integrity monitor. Since the DARE neglects the temporal convergence of the uncertainty of the estimator, the steady-state protection levels are consistently less than the actual protection levels, which is computed from standard sequential updates. The partial simulation of the protection levels only represents the geometric relations between the satellites, network receivers, and the user.

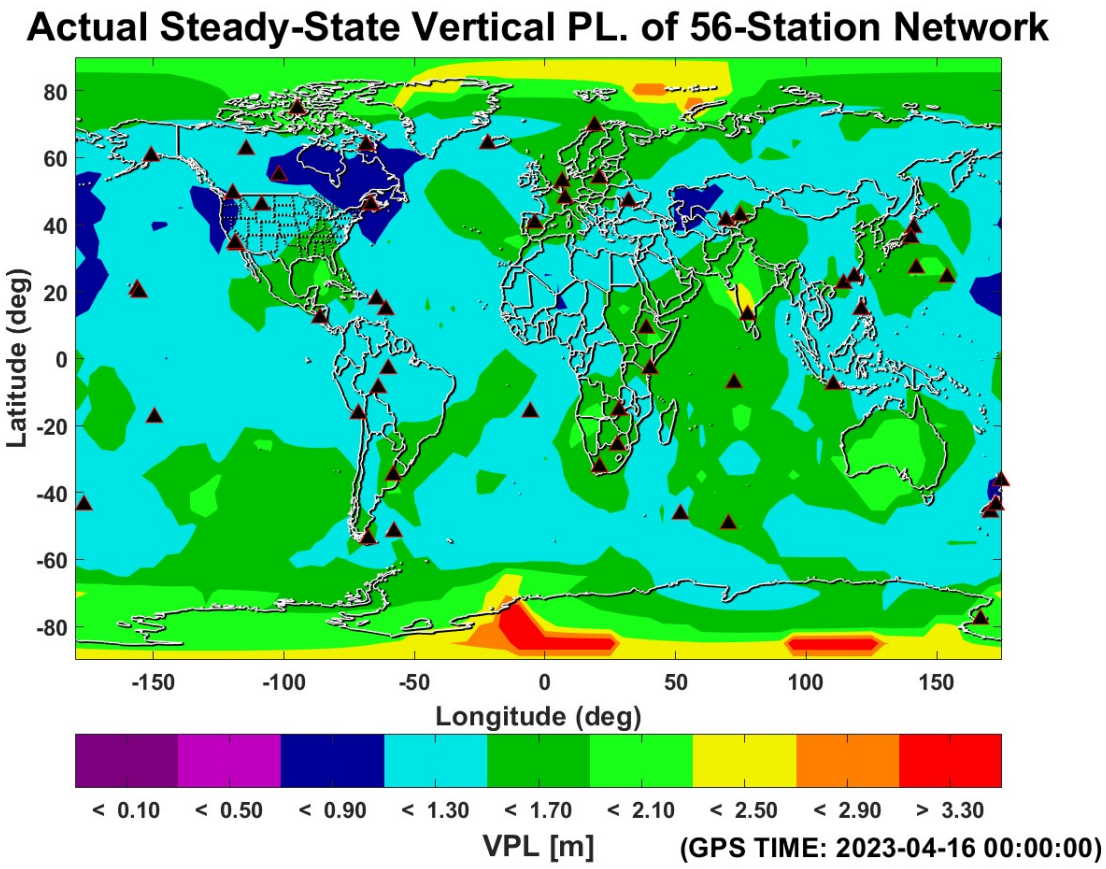

Figure 6: Steady-State snapshot VPL from real Network.

Fig.6 is the steady-state VPL of the 56-station network, where the black triangles represent the receiver location of network. The integrity information is computed from the actual IGS code/carrier phase data and precise product from the network receivers, and the global VPL map consists of the $5^\circ \times 5^\circ$ granularity grids. Each grid point is simulated as a PPP user applying the integrity information to its pseudoragne model with the precise ephemeris used by the integrity network at steady-state. It represents the minimal protection level that PPP users can achieve given the the integrity information from the actual network. The VPL map is a snapshot of the simulation on April 16$^{\text{th}}$, 2023 at 00:00:00.

We can see the steady-state performance of the potential PPP users at different locations on earth with the integrity information given by the 56-station network. In general, the users can achieve $1 \sim 2$ m of VPL at the moment in most part of the world, with slightly worse performance in India, much degraded VPL in Arctic and Antarctica regions. The global VPL map gives a clear view of how the integrity information from the integrity monitor affects the users around the world at an instance for which the protection level depends solely on the geometries between the satellites and the receivers.

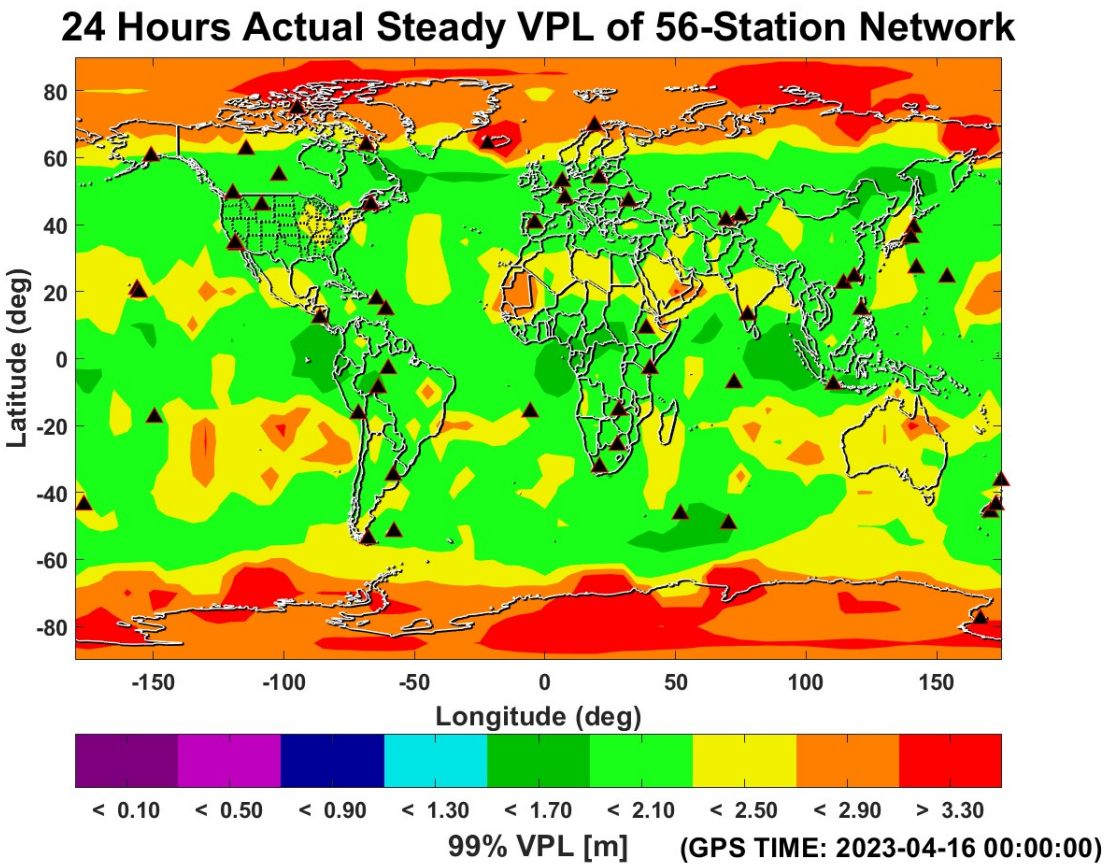

Figure 7: 99% availability of steady-state VPL from real Network.

Due to the movement of the satellite ephemerides, the LOS geometries of the satellites, receivers and users also constantly change, which would result in different protection levels for users at different times of a day. Fig.7 is the 99% availability of the VPL from the same 56-station network over 24 hours on April 16th. It shows the worst-case scenarios for distribution of the VPL on Earth 99% of the time on April 16th. In other words, 99% of the time the PPP users would experience VPLs lower than what is shown on Fig.7. The availability map combines the temporal evolvement and spatial variations of the protection levels at steady-state for PPP users at different part of the world over an extensive period time into a single plot. Since the GPS constellation has a period of about 12 hours, the geometries repeat at a period of approximately 24 hours, meaning that the steady-state protection levels would also repeat every 24 hours. It can be clearly seen that the 56-station network does not perform well in the North and South poles in terms of the VPL, and is relatively worse in regions like Australia, Middle East, Mexico etc., comparing to regions such as U.S., Europe and Southeast Asia. Originally, the design of the 56-station network did not consider the role of the users when selecting stations from the IGS network. As a result, the performance of the network for users located in different regions of the world is established arbitrarily. Therefore, the evaluation of the protection levels as shown in Fig.7 provides a direct view of what levels of service the integrity monitor can guarantee to the users. This is how the performance of a receiver network is evaluated in this paper.

2. Full Simulation

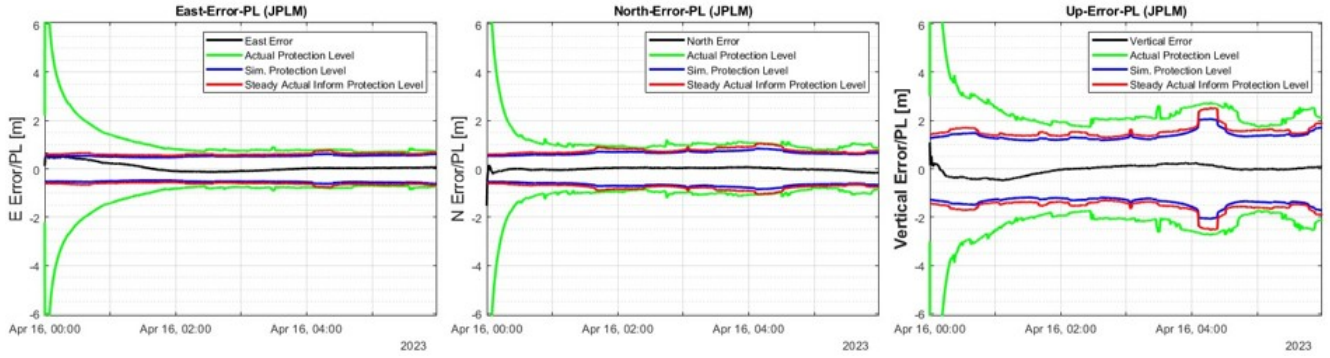

Figure 8: Full simulation of JPLM user.

Fig.8 is the full simulation of the JPLM user from the 56-station network. The blue lines are the final steady-state protection levels, where the ephemerides are simulated by the almanac, the user is simulated via 21, and the integrity information are computed from Eq.32. This is the lowest possible protection levels that the user can achieve given the geometric relations of the user, network receivers, satellites, and priors. Since the entire process involves no real data, it enables efficient computation of the user protection levels from the integrity monitor given any receiver network and users anywhere on earth.

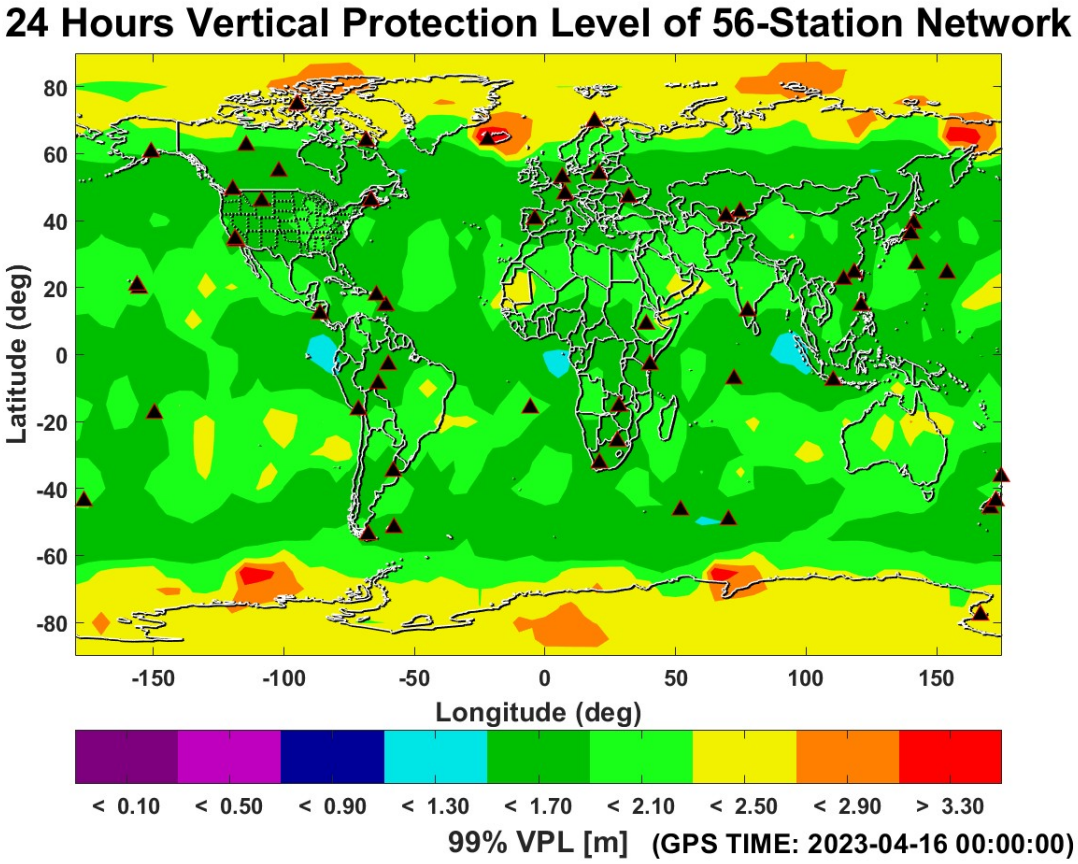

Figure 9: Steady-State VPL from real Network.

Similarly, Fig.9 is the 99% availability of the steady-state VPL of the 56-station network. The differences are the ephemerides

are simulated from the almanac and the integrity information is computed from the steady-state information filter approximation in Eq.32, whereas the VPL in Fig.7 is computed from the actual sequential Kalman filter with the measurements from the receiver network and ephemeris from the precise product.

As expected, the VPL of Fig.9 is consistently lower than the one with actual precise product in Fig.7 since Fig.9 is computed completely from simulation at steady-state. The only factor that would cut-off the LOS signals is elevation angles, so it is the lower bound protection levels PPP users can achieve from the given integrity network network. Nevertheless, the relative performance of the users in different regions of the Earth is still representative. We can see the users still have relatively poor VPL in the North and South poles, and regions such as Australia and Middle East still have relatively worse protection levels. The key point is that the evaluation of the integrity monitor is not reliant on the real data anymore, so we can evaluate the performance of any arbitrary combination of the receiver network to understand service regions of the integrity monitor in terms of protection level.

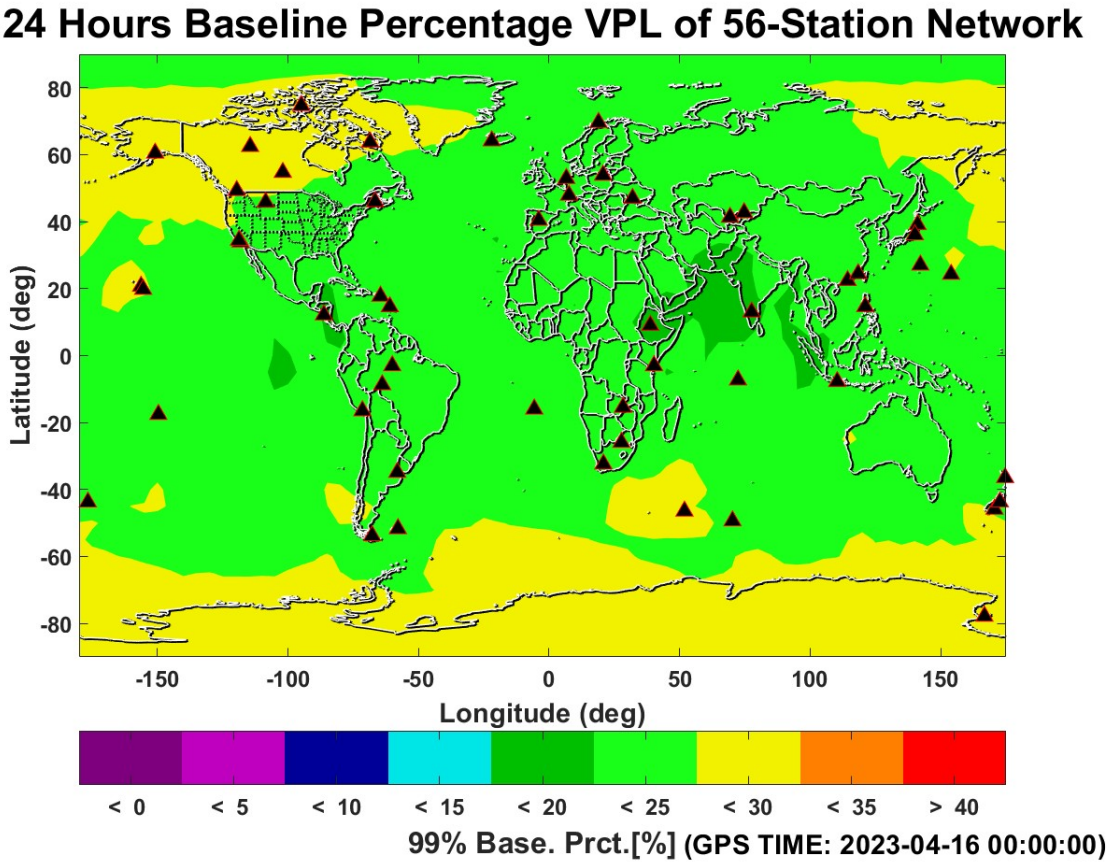

Figure 10: Steady-State VPL from real Network.

Define the baseline percentage as:

$$Baeline\ Prct. = \frac{VPL_{actual} - VPL_{almanac}}{VPL_{almanac}} \cdot 100\ [\%] \tag{33}$$

Fig.10 is the 99% availability of baseline percentage of the global VPL, where the almanac VPL (Fig.9) is the baseline and is compared with the VPL with actual integrity information(Fig.7). In general, 99% of the time on April 16th, the VPLs of the full simulation is less than 25% greater than the actual VPLs in latitude lower than $60°$, and are about 30% greater in latitude higher than $60°$. This indicates the approximation of the gap between the lower bound VPLs form the almanac simulation and the actual VPLs. Since the data from the real receivers might not always be available, the performance of a simulated receiver network with almanac ephemeris enables the approximation of the actual VPL even if there are no receivers placed in the field.

VI. CONCLUSION

In this paper, we evaluated the performance of a ground-based integrity network. The performance is defined to be the protection levels at any potential user location on earth. The temporal correlations are ignored via solving a steady-state Kalman filter when computing the protection levels for each potential user. Therefore, the performance of the integrity network is solely dependent on the relative geometry between receivers and satellites. 56 IGS stations are chosen to be an example network to demonstrate performance evaluation using their real code/carrier phase measurements and the precise products. Additionally, we derived the approximation of the steady-state satellite clock and ephemeris errors information equations that can easily compute the steady-state covariance of the error states given the LOS geometry, which can be specified by any combination of the network receivers. Combining with the ephemeris simulation using almanac data, we can rapidly evaluate arbitrary number and geometry of the receiver network.

Example results showed that users can generally achieve $1.5 \sim 2$ m VPL using the integrity information generated from the real network size of 56 stations, and $1.2 \sim 1.5$ m VPL if the integrity information is generated from almanac and Eq.32. The percentage differences of the former one is in general $25 \sim 30\%$ greater than the later one, which is essentially the lower bound of the VPL that a network can achieve. Given that the real data from the receivers are not easily accessible beforehand when designing a monitor network, the use of almanac and the steady-state approximation allows rapid performance evaluations of any network geometry choosing and placing receivers during the design of a ground-based integrity monitor.

ACKNOWLEDGEMENTS

We gratefully acknowledge the support of the FAA Satellite Navigation Team for funding this work under Memorandum of Agreement #: 693KA8-22-N-00015.

REFERENCES

IGS, M. (2026). International gnss service.

Jan, S.-S., Chan, W., and Walter, T. (2009). Matlab algorithm availability simulation tool. *GPS solutions*, 13(4):327–332.

Lai, Y.-F., Blanch, J., and Walter, T. (2024). Ground-based integrity monitors for ppp correction services. In *Proceedings of the ION 2024 Pacific PNT Meeting*, pages 514–526.

Lai, Y.-F., Blanch, J., and Walter, T. (2025a). Protecting against receiver faults to a ppp ground-based integrity monitor system. In *Proceedings of the 2025 International Technical Meeting of The Institute of Navigation*, pages 343–358.

Lai, Y.-F., Blanch, J., and Walter, T. (2025b). User range error corrections with latency from ppp ground-based integrity monitor system. In *Proceedings of the 38th International Technical Meeting of the Satellite Division of The Institute of Navigation (ION GNSS+ 2025)*, pages 178–191.

Welch, G., Bishop, G., et al. (1995). An introduction to the kalman filter.

Zumberge, J., Heflin, M., Jefferson, D., Watkins, M., and Webb, F. H. (1997). Precise point positioning for the efficient and robust analysis of gps data from large networks. *Journal of geophysical research: solid earth*, 102(B3):5005–5017.